ADVANCES IN ATMOSPHERIC SCIENCES, VOL. 43, MAY 2026, 965–980

• Original Paper •

Evaluation of Global NWP Data on the Convection Environment over the Data-Sparse Northern South China Sea by Long-Term Observations

Ling HUANG*[1], Zhiyong MENG[2], and Murong ZHANG[3]

[1]*Institute of Tropical and Marine Meteorology, China Meteorological Administration, Guangzhou, China*
[2]*Department of Atmospheric and Oceanic Sciences, School of Physics, and China Meteorological Administration Tornado Key Laboratory, Peking University, Beijing, China*
[3]*State Key Laboratory of Marine Environmental Science, Center for Marine Meteorology and Climate Change, College of Ocean and Earth Sciences, Xiamen University, Fujian, China*

(Received 19 June 2025; revised 2 September 2025; accepted 28 September 2025)

ABSTRACT

The coastal regions of southern China experience the country's most frequent convective weather. Accurately representing the low-level upstream atmospheric state over the data-sparse South China Sea (SCS) is crucial for reliable convection predictions in numerical models. Utilizing 10 years of radiosonde observations launched over the SCS, this study presents the upstream offshore convective environments and evaluates the global model data performance including NCEP FNL, ERA5, CRA-40, JRA-3Q, and MERRA-2. Results show that thermodynamic state variables such as temperature and humidity exhibit greater biases than kinetic variables, particularly at low levels. Deeper-layer parameters exhibit smaller uncertainties, especially wind-related variables, while moisture-related parameters have the largest uncertainties, compared to shallower-layer parameters. All model data tend to underestimate the conditional instability and equilibrium level, while overestimating the condensation level, storm relative helicity (SRH), with minimal bias in lapse rate, convective inhibition, vertical wind shear (VWS), and mean winds. These biases primarily arise from the model data's underestimation of temperature and moisture below 700 hPa and lower wind speeds below 950 hPa. Among the global models, CRA-40 performs best in dynamic parameters, with highest correlation and lowest mean absolute error in low-level winds, SRH, VWS, and mean winds. ERA5 excels in thermodynamic parameters. Additional convective-permitting numerical experiments indicate that minor initial condition errors over the upstream ocean significantly affect coastal rainfall production. The rainfall production on windward coasts is most sensitive to the low-level air temperature errors during nocturnal hours, while the rainfall over the PRD is most sensitive to the low-level wind errors.

Key words: Radiosonde, convective environments, rainfall, northern South China Sea

Citation: Huang, L., Z. Y. Meng, and M. R. Zhang, 2026: Evaluation of global NWP data on the convection environment over the data-sparse northern South China Sea by long-term observations. *Adv. Atmos. Sci.*, **43**(5), 965−980, https://doi.org/10.1007/s00376-025-5287-7.

Article Highlights:

- NWP data exhibit systematic bias under 950 hPa, with positive biases in V and negative biases in U, Q, and T.
- NWP data are least reliable for moisture parameters, followed by temperature parameters, and most reliable for wind parameters.
- CRA-40 performs best for wind-related parameters, while ERA5 excels in moisture- and temperature-related parameters.
- The rainfall production on windward coasts is most sensitive to the low-level air temperature errors during nocturnal hours.

1. Introduction

Located to the north of the South China Sea, the southern China coasts are densely populated and economically vital, making them highly vulnerable to extreme weather events like heavy rainfall (Fig. 1a), typhoons, and storm surges, particularly from April to September (Sun et al., 2019; Fu et al., 2022). Accurate forecasts are crucial for safeguarding lives and reducing economic losses. Previous studies have demonstrated that upstream environment over the northern South China Sea (NSCS) significantly influence downstream

* Corresponding author: Ling HUANG
Email: huangl_atmos@foxmail.com

© Institute of Atmospheric Physics/Chinese Academy of Sciences, and Science Press 2026

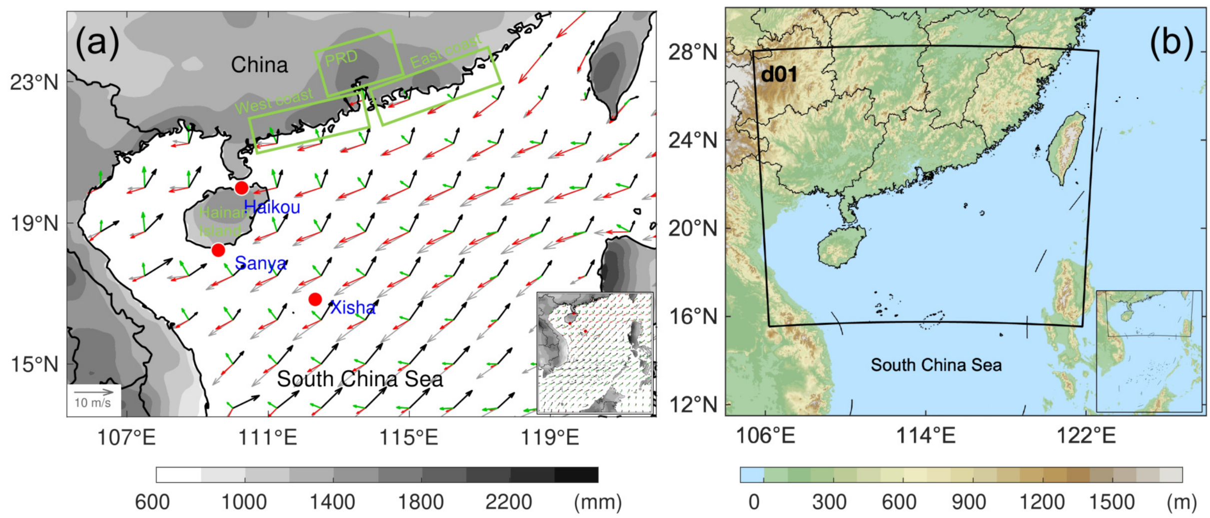

Fig. 1. (a) Distribution of seasonal wind vectors at 925 hPa of March to May (green vectors), June to August (black vectors), September to November (red vectors), and December to February (grey vectors), from 2014 to 2023. The color shading indicates the annual rainfall averaged from 2014 to 2023, obtained from IMERG. The red dots indicate the locations of soundings. The green rectangles indicate the hot spots of precipitation over the south coast of China: the west coast, the east coast, and the pearl river delta region (PRD). (b) Domain and topography of the simulations.

coastal weather, especially under monsoonal flow conducive to severe convection (Du and Chen, 2019). Understanding the low-level upstream atmospheric state over the data-sparse NSCS is critical for unrevealing mechanisms behind severe weather formation and development. An accurate representation of this state in numerical models is vital for enhancing the reliability of convection forecasts in downstream coastal regions.

Radiosonde observations have been widely used to study regional convective climatology, but they are spatially and temporally limited (Bao and Zhang, 2013; Allen and Tippett, 2015; Tippett et al., 2016; Taszarek et al., 2017, 2018; Virman et al., 2021). Numerical weather prediction (NWP) models provide a more comprehensive, high-resolution four-dimensional view of the atmosphere and are particularly beneficial for analyzing sensitive parameters like storm-relative helicity (SRH) or CAPE (Markowski et al., 1998). Spatiotemporal climatologies of severe convective environments based on NWP data have been investigated globally (e.g., Rädler et al., 2018; Taszarek et al., 2018, 2020, 2021; Chen et al., 2020; Varga and Breuer, 2022), which reveal regionally dependent features across continents. For instance, Taszarek et al. (2018) noted CAPE underestimation in eastern Europe and overestimation in the Mediterranean. Over the mainland of China, Wu et al. (2024) observed CAPE overestimation 2 h before rainfall onset. These findings underscore the need to assess NWP data quality for specific regions before applying them to research or forecasting.

While satellite data have enhanced upper and mid-tropospheric analysis, their reliability in resolving low-level thermodynamic and dynamic profiles—critical for understanding local convective environments—remains uncertain due to sparse observational constraints (e.g., Davis et al., 2017; Manney et al., 2017). For thermodynamic parameters, large errors in low-level temperature and moisture fields are noticed in NWP datasets, such as ERA-Interim (Allen and Karoly, 2014), NCEP/NCAR reanalysis (Lee, 2002), and RUC-2 (Thompson et al., 2003). For dynamics, Taszarek et al. (2018) found underestimation of low-level vertical wind shear (VWS) in ERA-Interim compared to sounding. Similarly, WRF simulations show biases in low-level jet placement and wind speed over the SCS and inland regions (Zhang and Meng, 2019). Yin et al. (2023) reported larger RMSEs in ERA-Interim zonal (U) and meridional (V) winds at low levels over East Asia. Uncertainty persists regarding the quantitative impact of low-level environmental errors on the convective environment.

Over the past two decades, the convective environments (Allen and Karoly, 2014; King and Kennedy, 2019; Li et al., 2020; Taszarek et al., 2021; Pilguj et al., 2022; Varga and Breuer, 2022) in global NWP datasets and comparisons among various NWP datasets (Taszarek et al., 2021; Varga and Breuer, 2022) have been assessed across regions. Varga and Breuer (2022) found that while WRF captures the seasonal cycle of thunderstorm predictors over Central Europe, its errors are higher than ERA5. Taszarek et al. (2021) analyzed millions of rawinsonde profiles against ERA5 and MERRA-2, finding ERA5 to be generally more accurate. The ERA5 data have been demonstrated to have higher correlations and lower mean absolute errors than MERRA-2 in terms of convective parameters and their trends (Pilguj et al., 2022). Each of the evaluated NWP data showed strengths and weaknesses, but broadly, they were found to adequately replicate the background convective environments.

Recently released reanalyses—JRA-3Q (Kosaka et al., 2024) and CRA-40 (Liu et al., 2023)—show promising improvements but have not yet been comprehensively assessed for convective environments. Harada et al. (2021) presented early evaluation results of JRA-3Q, showing its enhanced precipitation representation, reduced tropical dry biases, and improved diabatic heating, compared to its previous version (JRA-55), likely due to better physical parameterizations (Kosaka et al., 2024). CRA-40, developed by the China Meteorological Administration (CMA), shows some advantages over China in terms of precipitation (Zhou et al., 2023), surface air temperature (Yang et al., 2021), humidity (Zhang et al., 2021), wind speed (Shen et al., 2022), tropical divergent kinetic energy (Li et al., 2023), and the Asian subtropical westerly jet stream (Yu et al., 2021). These results suggest that the improvement of CRA-40 and JRA-3Q allows for an excellent representation of weather systems; however, they have yet to be explored for convective environments.

While global NWP datasets can replicate temperature, specific humidity, and wind profiles, biases remain nontrivial and may exceed regional climate signal magnitudes (e.g., Bao and Zhang, 2013; Pilguj et al., 2022). The effects of these initial and boundary condition errors on high-impact weather events like heavy rainfall have been explored in case studies using data assimilation and ensemble forecasts (e.g., Tootill and Kirshbaum, 2022), including torrential rainfall over South China (e.g., Gao et al., 2022; Bao et al., 2023). However, the climatological impact of such errors on convection remains poorly understood.

Convective predictability over southern China coasts remains relatively low (e.g., Huang and Luo, 2017). Given the NSCS's importance to coastal convection (e.g., Ding and Chan, 2005), this study aims to (1) investigate the climatology of convective parameters over the NSCS using 10 years of high-quality sounding data; (2) evaluate convective parameters from five widely used NWP datasets; and (3) investigate how initial and boundary condition errors in these datasets influence convection prediction from a climatological perspective. Section 2 introduces the datasets. Section 3 presents the evaluation through basic state quantities, thermodynamic parameters, and dynamic parameters. Section 4 explores the impact of initial and boundary condition errors on coastal convections. A summary and discussion are provided in section 5.

2. Data and methods

2.1. *Radiosonde observations*

The vertical atmospheric profiles were derived from three soundings over the NSCS (Fig. 1a). For the years 2014–23, all available measurements comprise 20793 soundings. However, to ensure the quality of the sounding data, strict quality-control procedures, including consistency checks, discrete value checks, monotonicity checks, stagnation value checks, and limit value checks, were performed. Specifically, the limit values for pressure, temperature, and wind speed are 0.1–1050 hPa, −100°C to 60°C, and 0–180 m s^{-1}. Given the inconsistency between the sounding and NWP data profile levels, the coarser soundings profiles are interpolated into the denser levels[a] through spline interpolation. Of note is that the data under 925 hPa are missing for Sanya station since its balloon drop point started from 419.4 m above sea level. Thus, the data at 1000, 975, and 950 hPa are set to missing values for Sanya profiles.

Also of note is that two of them (Haikou and Xisha stations) have been incorporated into the reanalysis processes through the Global Telecommunication System program. Even though NWP reanalysis combines observations and numerical models to produce the best estimate of the atmospheric state, simulated biases inevitably persist due to the constraints of physical balance during the data assimilation process (Taszarek et al., 2021). A possible reason is that the soundings are launched over land on a small island, whereas the NWP data may represent the corresponding grid point as more oceanic (Virman et al., 2021).

2.2. *NWP datasets*

Five modern global NWP datasets were employed—namely, CRA-40 from the CMA (Liu et al., 2023), JRA-3Q from the Japanese Meteorological Administration (Kosaka et al., 2024), FNL from the NCEP Global Forecast System (GFS; National Centers for Environmental Prediction/National Weather Service/NOAA/U.S. Department of Commerce, 2000), MERRA-2 from NASA's Global Modeling and Assimilation Office (GMAO; Gelaro et al., 2017), and ERA5 from ECMWF (Hersbach et al., 2020). CRA-40, China's first-generation reanalysis, offers six-hourly data at a 34 km resolution with 64 vertical levels, including eight below 2 km. JRA-3Q provides a 40 km resolution and 100 vertical layers, with 23 below 2 km. FNL offers 1° × 1° data every six hours with 26 vertical levels, six of which are below 2 km. MERRA-2 has a 0.5° × 0.625° resolution, three-hour intervals, and 72 levels (14 below 2 km). ERA5 features a 0.25° resolution and 137 vertical levels, including 28 in the lowest 2 km. To enable comparison, a set of standard pressure levels[a], with a focus on low-level layers, is used across all datasets. Coarser data, such as FNL, are interpolated into these standard levels using spline interpolation. The soundings of the NWP are derived from the grid points nearest to the station, which resemble profiles of the nearby environment (not shown).

2.3. *Convective parameters*

The parameters evaluated were selected based on commonly used indices in severe thunderstorm environments (e.g., Taszarek et al., 2021). These include thermodynamic parameters like surface-based (SB) parcel parameters (SBCAPE, SBCIN, and LCL) and lapse rates (LRs) between different bulk layers ($LR_{0–1km}$, $LR_{0–3km}$, and $LR_{500–700hPa}$), as well as dynamic parameters such as VWS ($VWS_{0–1km}$, $VWS_{0–3km}$, $VWS_{0–6km}$), SRH ($SRH_{0–1km}$,

[a]The pressure levels used in the current study are 1000, 975, 950, 925, 900, 875, 850, 825, 800, 775, 750, 700, 650, 600, 500, 400, 300, 200, 100 hPa.

$SRH_{0–3km}$), and mean wind ($MW_{0–1km}$, $MW_{0–3km}$, and $MW_{0–6km}$; Table 1). VWS and MW were calculated using wind differences or averages between 10 m and the heights of 1, 3, and 6 km AGL. All the parameters were computed using the same script across the datasets (sounding, ERA5, CRA-40, MERRA-2, JRA-3Q, and FNL) to ensure consistency. Due to the limited data below 925 hPa at Sanya station, its SB parameters were excluded.

2.4. *Design of semi-idealized numerical experiments*

Various NWP models are expected to introduce varying degrees of bias. To assess how these biases affect coastal convection and its associated rainfall in downstream regions, periodic convection-permitting simulations were conducted. The aim of these simulations was not to replicate specific events but to assess how background state errors influence general rainfall patterns during the rainy season. Periodic simulations use averaged initial and boundary conditions to isolate the impact of these errors while preserving daily diurnal cycles, such as land–sea breezes. The control experiment (CTL) used a 10-day simulation with the 549-day-averaged FNL data (from 1 April to 30 September 2020–23) as initialization at 0000 UTC and repeated boundary conditions at 0000, 0600, 1200, and 1800 UTC. This setup removed temporal variability while retaining daily diurnal features, enabling simulation of typical diurnal driven precipitation, as used in previous studies (e.g., Sun and Zhang, 2012; Chen et al., 2016). It should be noted that the purpose of these simulations was to investigate how different error types affect convection and associated precipitation. FNL has known typical errors, especially for low-level dynamic parameters (section 3.2.1), making it a suitable choice for the initial and boundary conditions in our periodic simulation.

Simulations used the WRF-ARW model (V4.5; Skamarock et al., 2008) over a single domain covering South China and the NSCS, with 400 × 330 horizontal grid points at 4 km grid spacing (Fig. 1b) and 51 vertical layers up to 50 hPa. Key physics schemes included YSU (Hong et al., 2006), Noah-MP (Niu et al., 2011), 5-layer thermal diffusion (Chen and Dudhia, 2001), WDM6 (Hong et al., 2004), the Grell–Devenyi ensemble (Grell and Dévényi, 2002), and RRTMG (Mlawer et al., 1997) for both longwave and shortwave radiation.

Sensitivity experiments of the semi-idealized periodic simulations were designed by subtracting vertical biases in *U*, *V*, temperature (*T*), and relative humidity (RH), either individually or combined, over the NSCS. These errors, based on April–September 2020–23 station-mean profiles (similar to April–September 2014–23), were further incorporated into the oceanic region. Subtracting these climatological errors helped align the model input with observations. Five sensitivity experiments were conducted (Table 2), including the "add_T_RH_U_V" experiment to test the combined effects, and "add_T" to isolate the influence of temperature.

3. Results

3.1. *General characteristics of atmospheric states calculated using radiosondes*

3.1.1. *Basic states*

Figure 2 presents the vertical profiles and seasonal variations of radiosonde-derived meteorological variables. From April to September, low-level winds are characterized by southerly components, which strengthen in April, peak in June with the South China Sea monsoon outbreaks (Li and Yanai, 1996), and weaken by July (Fig. 2a). Temperature and humidity also vary monthly, with cooler, drier conditions before the monsoon and warming/increased humidity as it pro-

Table 1. List of some of the common abbreviations and acronyms used in this paper.

Abbreviation	Stands for	units
AGL	Above ground level	m
SBCAPE	Surface-based convective available potential energy	J kg^{-1}
SBCIN	Surface-based convective inhibition	J kg^{-1}
LCL	Level of free convection	m
EL	equilibrium level	m
LFC	Level of free convection	m
$LR_{0–1km}$	Lapse rate from 0 to 1 km	K m^{-1}
$LR_{0–3km}$	Lapse rate from 0 to 3 km	K m^{-1}
$LR_{700–500hPa}$	Lapse rate from 700 to 500 hPa	K hPa^{-1}
$VWS_{0–1km}$	Vertical wind shear between 0 and 1 km AGL	m s^{-1}
$VWS_{0–3km}$	Vertical wind shear between 0 and 3 km AGL	m s^{-1}
$VWS_{0–6km}$	Vertical wind shear between 0 and 6 km AGL	m s^{-1}
$SRH_{0–1km}$	Storm relative helicity between 0 and 1 km	m^2 s^{-2}
$SRH_{0–3km}$	Storm relative helicity between 0 and 3 km	m^2 s^{-2}
$MW_{0–1km}$	Mean wind speed between 0 and 1 km	m s^{-1}
$MW_{0–3km}$	Mean wind speed between 0 and 3 km	m s^{-1}
$MW_{0–6km}$	Mean wind speed between 0 and 6 km	m s^{-1}

gresses (Figs. 2e, f). The zonal wind shifts from easterly (April–May) to westerly (June–August), then back to easterly in September (Fig. 2b), causing a total wind direction transition from southeasterly to southwesterly (Fig. 2c). A strong low-level jet appears near 950 hPa from April to August (Fig. 2d), linked to intensified southerlies (Fig. 2a). This pattern suggests low-level air affecting coastal South China originates mainly from the NSCS (Fig. 1a).

3.1.2. *Convective environments*

Situated in the tropical ocean, the NSCS has high conditional instability, with a mean SBCAPE reaching 1500 J kg^{-1}, much higher than Europe and North America (250 J kg^{-1}; Taszarek et al., 2021). The SBCAPE rises with the onset of monsoonal flow in late May, peaks during the outbreaks of monsoonal flow in June, and remains high in July and August (Fig. 3a). As the monsoonal flow strengthens, SBCIN drops below 50 J kg^{-1} (Fig. 3b), and $LR_{0–3km}$ rises to ~5.5°C km^{-1} from June onward (Fig. 3c). LCL values, though lower than in Europe and North America (Taszarek et al., 2021), show little monthly change (Fig. 3c). This combination of high SBCAPE, moderate SBCIN, low LCL, and steep LR create favorable conditions for convection with a lower cloud base.

Comparisons of the monthly variations of dynamic parameters indicate the potential for organized severe weather systems (Fig. 4). Large SRH and deep-layer VWS are found in April, supporting the development of damaging rotating storms such as supercells (Figs. 4a–4d; Davies-Jones et al., 1990). Yet, convection is relatively infrequent in April compared to subsequent months, mostly due to the less favorable thermodynamic environment indicated by SBCAPE (Fig. 3d). From May to September, the low-level mean VWS computed from the surface to 1 km and 6 km is around 3.2 and 6.5 m s^{-1}, respectively. Such VWS (> 5 m s^{-1}; Feng and Zhang, 2018) favors long-lived,

Table 2. Design of the sensitivity experiments.

Experiment	Design
CTL	Simulation using periodic initial and boundary conditions averaged from April to September 2020–23
add_T_RH_U_V	Similar to CTL but errors of *T*, RH, *U*, and *V* from 1000 to 700 hPa were subtracted in the initial and boundary conditions over the ocean
add_T	Similar to add_T_RH_U_V but only the *T* errors were introduced
add_RH	Similar to add_T_RH_U_V but only the RH errors were introduced
add_T_RH	Similar to add_T_RH_U_V but only the RH and *T* errors were introduced
add_U_V	Similar to add_T_RH_U_V but only the *U* and *V* errors were introduced

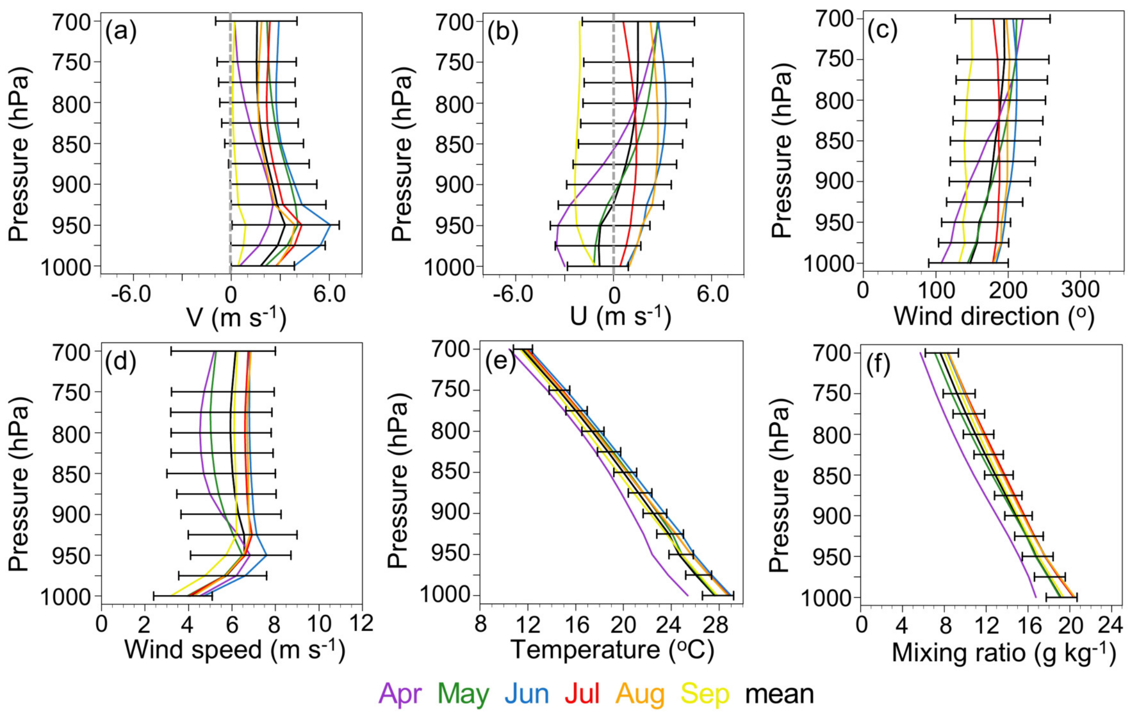

Fig. 2. Vertical profiles of average (a) meridional wind (units: m s^{-1}), (b) zonal wind (units: m s^{-1}), (c) wind direction (units: °), (d) total wind speed (units: m s^{-1}), (e) temperature (units: °C), and (f) water vapor mixing ratio (units: g kg^{-1}) obtained from the radiosonde observations. The error bars show the outliers (i.e., 10th and 90th percentiles are whiskers).

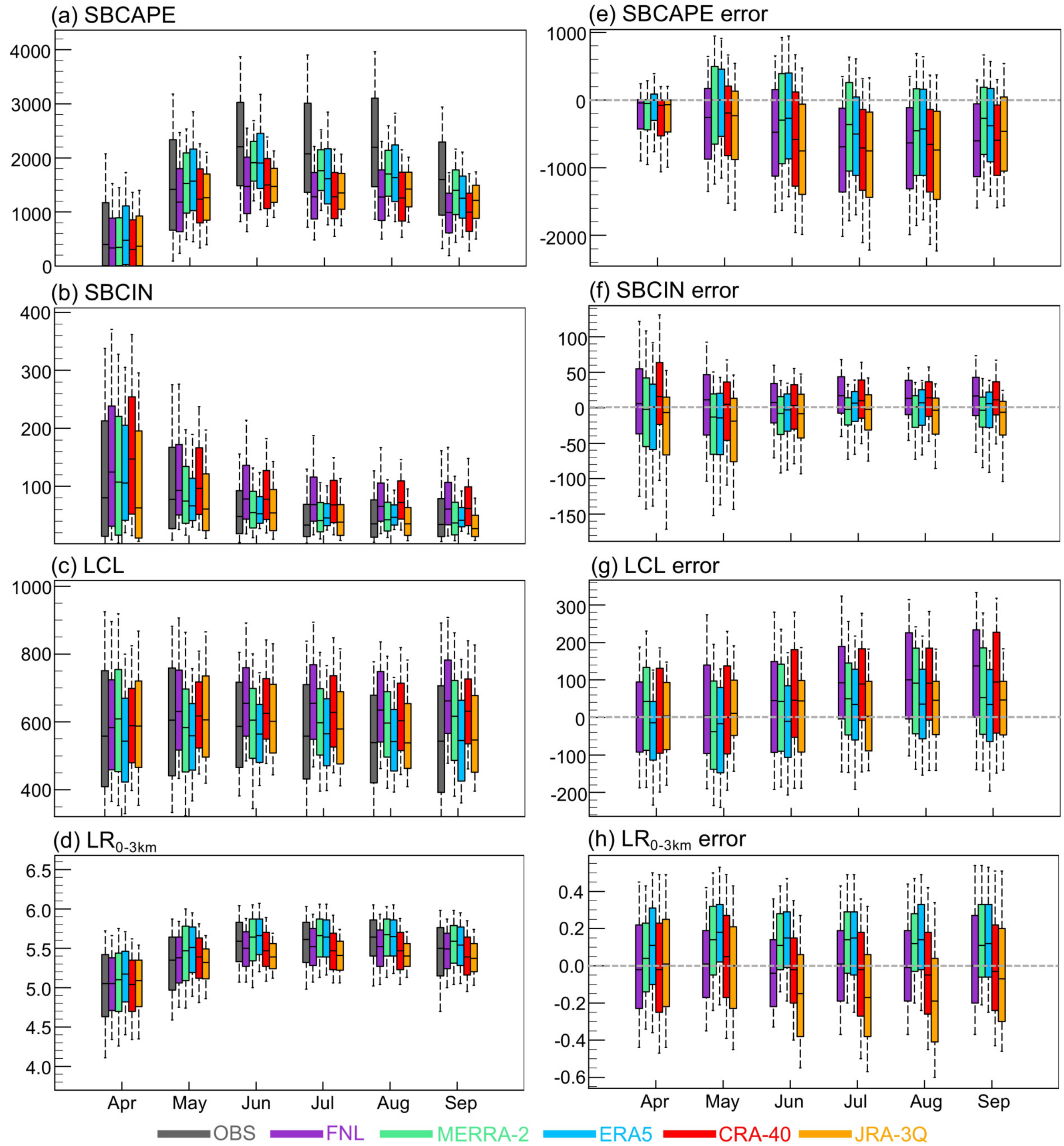

Fig. 3. Comparison of monthly variation of (a) SBCAPE (units: J kg^{-1}), (b) SBCIN (units: J kg^{-1}), (c) LCL (units: m), and (d) LR_{0-3km} (units: °C m^{-1}) from the NWP data and observation, and (e–h) NWP errors respective to the observation (NWP data minus observation).

moderate-speed, and moderate-sized rainfall systems with high rain rates (Baidu et al., 2022).

3.2. *Performance of the NWP data*

3.2.1. *Basic states*

The basic states of five global NWP datasets are evaluated against climatological profiles from three radiosondes using the mean bias and RMSE (Fig. 5). All NWP data exhibit a negative bias in *U* winds (Fig. 5a) and a positive bias in *V* winds (Fig. 5b) below 925 hPa, decreasing to nearly 0 by 700 hPa, consistent with Yin et al. (2023) and Zhang and Meng (2019). Specifically, *U* winds are underestimated by 0.4–0.6 m s^{-1} and *V* winds are overestimated by 0.6–1.0 m s^{-1} below 925 hPa, leading to an overestimation by ~1 m s^{-1} in wind speeds (Fig. 5c). The RMSEs are generally within acceptable limits for assimilation, except that for wind direction (Fig. 5d). For thermodynamic state variables, temperature shows a cold bias peaking at 950–925 hPa (Fig. 5e), while humidity errors peak at 1000 and 900 hPa, with positive biases above 750 hPa (Fig. 5f). The low-level thermodynamic errors are common in global datasets, as

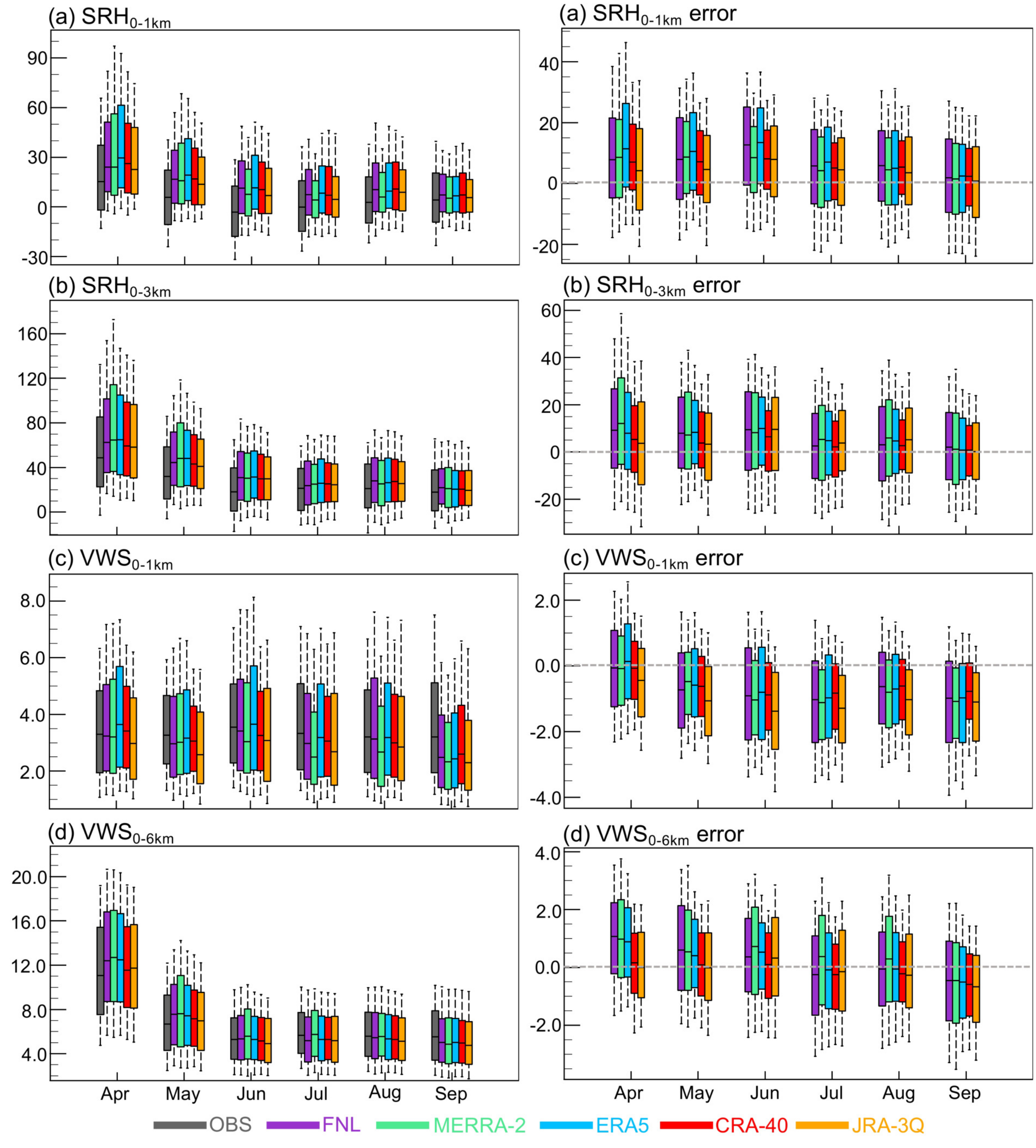

Fig. 4. Similar to Fig. 3 but for (a, e) $SRH_{0–1km}$ (units: $m^2 s^{-2}$), (b, f) $SRH_{0–3km}$ (units: $m^2 s^{-2}$), (c, g) $VWS_{0–1km}$ (units: m s^{-1}), and (d, h) $VWS_{0–6km}$ (units: m s^{-1}).

seen in ERA-Interim (Allen and Karoly, 2014), NCEP/NCAR (Lee, 2002) and RUC-2 (Thompson et al., 2003), even with the sounding data having been incorporated in the NWP model.

Among the datasets, CRA-40 performs best for dynamic state parameters, showing the highest correlation for U and V wind components, especially above 825 hPa (Table 3), though still biased near the surface (Figs. 5a, b). ERA5 leads in thermodynamic accuracy, especially for the water vapor mixing ratio (Q_v) below 925 hPa, and provides unbiased Q_v profiles above 800 hPa (Fig. 5f). As for temperature, both ERA5 and CRA-40 show strong correlation with observations at key levels (Table 3), while MEERA-2 has smaller mean errors below 850 hPa (Fig. 5e, Table 3). In summary, ERA5 best captures nonlinear variables like Q_v, while CRA-40 and MERRA-2 excel in linear state variables. Despite these difference, overall deviations are modest, at under 0.8 m s^{-1} for U, 0.4 m s^{-1} for V, 1°C for temperature, and 1 g kg^{-1} for Q_v.

3.2.2. *Composite parameters*

Thermodynamic performance over the NSCS is first com-

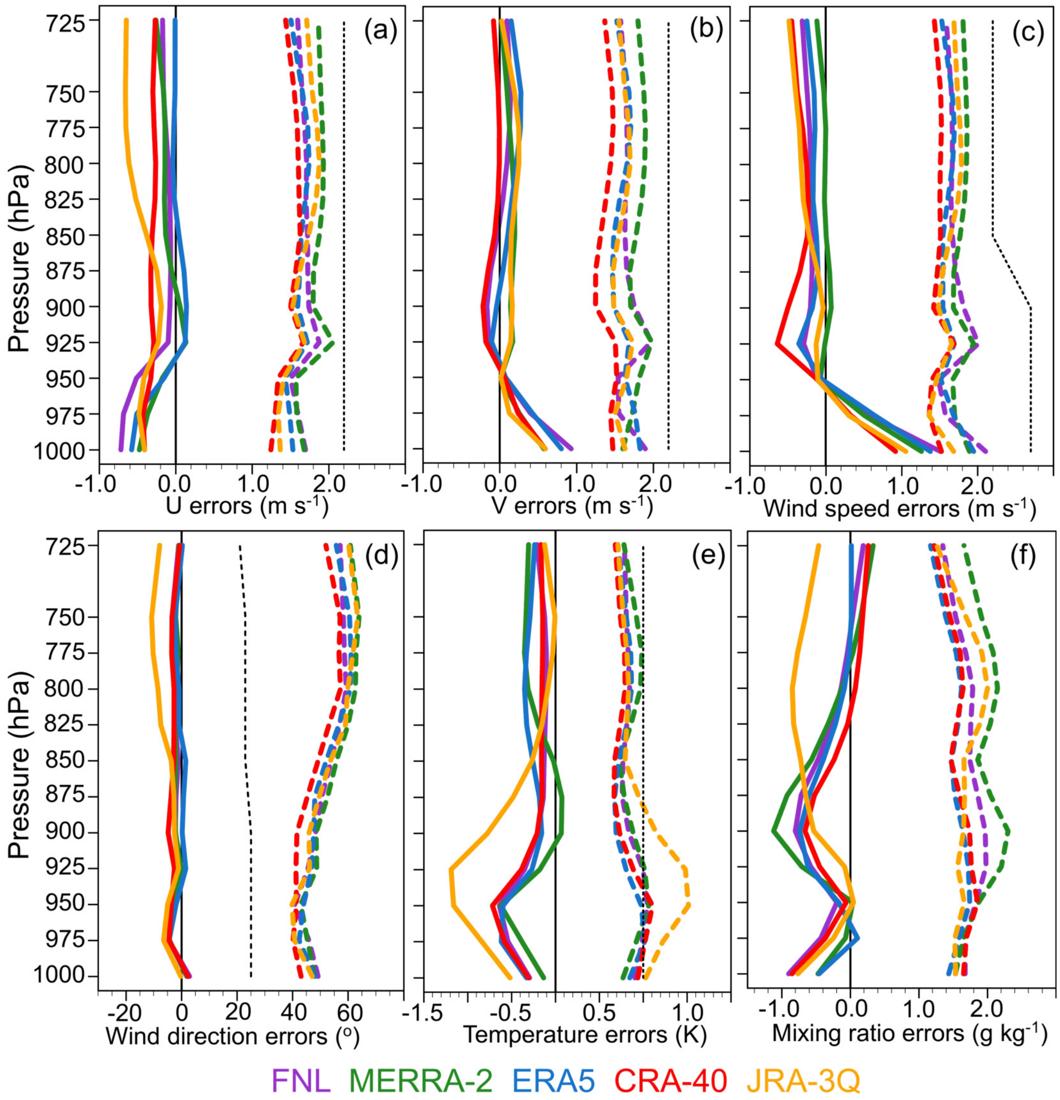

Fig. 5. Vertical profiles of mean errors (solid lines) and RMSE (dashed lines) for (a) zonal winds (units: m s^{-1}), (b) meridional winds (units: m s^{-1}), (c) total wind speed (units: m s^{-1}), (d) wind direction (units: °), (e) temperature (units: °C), and (f) water vapor mixing ratio (units: g kg^{-1}). The errors are derived by the difference between NWP soundings and observational soundings (NWP minus observation). The black thick dashed lines in (a–e) denote the standard sounding observation errors for the NCEP model (Bao and Zhang, 2013).

pared to that over Europe and North America. Median error analysis reveals NWP datasets consistently underestimate SBCAPE and overestimate LCL (Fig. 3e, Table 4), aligning with studies over North America (King and Kennedy, 2019; Taszarek et al., 2021). In contrast, SBCAPE tends to be overestimated over Europe (Taszarek et al., 2021; Varga and Breuer, 2022), indicating regional variability in NPW accuracy. SBCAPE errors range widely, from near-zero (ERA5) to −297.9 (FNL), indicating substantial uncertainties in this moisture- and temperature-sensitive composite parameter. Uncertainties in SBCIN and LR are even larger and vary with season and dataset.

Further analysis of thermodynamic parameters suggests low-level moisture is the main source of instability uncertainties. NWP datasets simulate temperature more accurately than moisture, with temperature correlations exceeding 0.9 at 925–850 hPa and the MAE being under 0.8 K (except for JRA-3Q) below 700 hPa. In contrast, Q_v exhibits weaker correlation (~0.7–0.8) and larger MAE, up to 1.67 g kg^{-1} at 925 hPa (MERRA-2), supporting previous findings that low-level moisture drives instability biases (e.g., Lee, 2002; Thompson et al., 2003; Allen and Karoly, 2014).

Among the datasets, ERA5 performs best for SBCAPE, with a near-zero median error (Fig. 3e), an MAE of −4.95 J kg^{-1}, and the highest correlation (0.65; Table 4), closely followed by MERRA-2, which can plausibly be attributed to the better presentation by ERA5 and MERRA-2 of T and Q_v under 950 hPa (Table 3, Fig. 5). CRA-40, JRA-3Q, and FNL exhibit larger biases, with median errors up to −400 J kg^{-1} and MAEs exceeding 400 J kg^{-1} (Fig. 3e,

Table 3. Pearson correlation coefficient, mean absolute error (MAE), and mean error (ME) comparing soundings with collocated FNL, MERRA-2, ERA5, CRA-40, and JRA-3Q for U (units: m s^{-1}), V (units: m s^{-1}), T (units: K), and Q_v (units: g kg^{-1}) at 925, 850, and 700 hPa. The best samples are highlighted in **bold**. The correlations have all passed significance testing at the 99% confidence level.

		Pearson correlation coefficient					Mean absolute error (MAE)					Mean error (ME)				
		FNL	MERRA-2	ERA5	CRA-40	JRA-3Q	FNL	MERRA-2	ERA5	CRA-40	JRA-3Q	FNL	MERRA-2	ERA5	CRA-40	JRA-3Q
925 hPa	U	0.94	0.93	0.95	**0.96**	0.95	1.31	1.45	1.20	**1.09**	1.18	**−0.10**	0.13	0.12	−0.29	−0.23
	V	0.90	0.90	0.92	**0.94**	0.92	1.36	1.38	1.16	**0.98**	1.19	−0.14	0.17	**−0.11**	−0.18	0.14
	T	0.92	0.92	**0.94**	**0.94**	0.91	0.79	0.77	**0.62**	0.70	1.27	−0.35	**−0.18**	−0.27	−0.39	−1.19
	Q_v	0.65	0.62	**0.76**	0.72	0.73	1.53	1.67	**1.31**	1.36	1.17	−0.58	−0.71	−0.62	−0.45	**−0.08**
850 hPa	U	0.95	0.94	0.95	**0.96**	0.95	1.23	1.37	1.16	**1.06**	1.26	−0.07	−0.13	**0.04**	−0.31	−0.38
	V	0.91	0.90	0.92	**0.94**	0.92	1.21	1.32	1.11	**0.92**	1.16	**−0.03**	0.19	0.10	−0.07	0.15
	T	0.93	0.94	0.94	**0.95**	0.89	0.58	0.52	0.54	**0.51**	0.60	−0.13	**−0.02**	−0.26	−0.16	−0.27
	Q_v	0.78	0.76	**0.84**	**0.84**	0.76	1.30	1.39	1.08	**1.06**	1.25	−0.47	−0.57	−0.40	**−0.24**	−0.73
700 hPa	U	0.96	0.94	0.96	**0.97**	0.96	1.20	1.39	1.10	**1.00**	1.29	−0.17	−0.26	**−0.01**	−0.27	−0.65
	V	0.93	0.91	0.93	**0.95**	0.93	1.16	1.31	1.10	**0.96**	1.13	0.09	**0.02**	0.15	−0.08	**0.02**
	T	0.85	0.87	0.87	**0.89**	0.86	0.60	0.59	0.54	**0.51**	0.53	−0.21	−0.31	−0.24	−0.17	**−0.12**
	Q_v	0.85	0.78	**0.88**	**0.88**	0.87	0.98	1.20	**0.84**	**0.84**	0.95	0.19	0.33	**0.01**	0.26	−0.46

Table 4. Similar to Table 2 but for composite parameters.

		Pearson correlation coefficient					Mean absolute error (MAE)					Mean error (ME)				
		FNL	MERRA-2	ERA5	CRA-40	JRA-3Q	FNL	MERRA-2	ERA5	CRA-40	JRA-3Q	FNL	MERRA-2	ERA5	CRA-40	JRA-3Q
Thermodynamic parameters	SBCAPE	0.64	0.65	0.65	**0.66**	0.65	498	446	445	458	**443**	−297.9	−42.66	**4.95**	−272.0	−100.9
	SBCIN	0.60	0.60	0.61	**0.62**	0.61	68.4	65.6	67.4	**60.7**	69.4	13.52	−22.00	−37.99	**0.54**	−50.51
	LCL	0.79	0.80	0.84	0.81	**0.91**	173	157	129	160	**105**	89.41	42.25	**−25.37**	56.08	27.34
	LFC	0.46	**0.49**	0.42	0.46	**0.49**	1150	**980**	1034	1020	981	545.8	−141.5	−220.1	402.9	**−104.9**
	EL	0.89	0.88	0.89	0.88	**0.90**	1482	1265	1229	1365	**1226**	−722.2	−132.4	−155.0	−648.0	**−98.8**
	$LR_{0–1km}$	0.76	0.77	0.78	**0.80**	0.69	1.20	**1.11**	1.23	1.17	1.57	0.49	**0.39**	0.49	0.41	1.19
	$LR_{0–3km}$	0.85	**0.86**	**0.86**	**0.86**	0.85	0.37	**0.35**	0.41	0.40	0.39	**0.13**	0.15	0.20	**0.13**	0.16
	$LR_{700–500hPa}$	0.86	**0.87**	0.86	0.86	0.85	0.41	**0.34**	**0.34**	**0.34**	0.35	0.06	−0.04	0.02	**0.00**	0.16
Dynamic parameters	$SRH_{0–1km}$	0.80	0.80	0.78	**0.88**	0.81	23.0	23.8	23.2	**18.0**	19.2	6.56	10.62	11.00	7.33	**5.09**
	$SRH_{0–3km}$	0.90	0.89	0.90	**0.92**	0.89	25.4	29.2	23.6	**20.0**	22.5	5.75	12.73	7.36	3.33	**1.94**
	$VS_{0–1km}$	0.59	0.62	0.60	**0.76**	0.69	1.85	1.64	1.63	**1.33**	1.51	−0.53	−0.40	**−0.27**	−0.55	−0.74
	$VS_{0–3km}$	0.88	0.87	0.89	**0.91**	0.90	1.88	2.00	1.68	**1.42**	1.52	**0.02**	0.67	0.18	−0.41	−0.71
	$VS_{0–6km}$	0.96	0.96	**0.97**	**0.97**	**0.97**	1.88	1.99	1.69	**1.42**	1.45	**0.18**	0.52	0.25	−0.36	−0.33
	$MW_{0–1km}$	0.88	0.88	**0.91**	0.90	**0.91**	1.14	1.11	1.00	**0.78**	0.89	0.28	0.56	0.47	**0.18**	0.29
	$MW_{0–3km}$	0.92	0.92	0.92	**0.93**	0.92	0.68	0.72	0.68	**0.55**	0.71	**0.01**	0.20	0.07	−0.08	0.06
	$MW_{0–6km}$	**0.95**	**0.95**	**0.95**	**0.95**	**0.95**	0.63	0.64	0.58	**0.56**	0.64	−0.19	**−0.00**	−0.07	−0.28	−0.19

Table 4). ERA5 also best estimates the LCL, while FNL and CRA-40 tend to overestimate it (Fig. 3g), resulting in less favorable conditions for convection. While FNL and CRA-40 generally overestimate the SBCIN, ERA5, MERRA-2 and JRA-3Q display a tendency toward underestimation (Fig. 3f).

While ERA5 tends to perform best for the nonlinear parameters, JRA-3Q, CRA-40 and MERRA-2 perform better for less nonlinear metrics. Specifically, JRA-3Q shows the best performance for EL and LFC, while CRA-40 and MERRA-2 best capture LRs (Table 4). ERA5's strength in capturing moisture- and temperature-dependent parameters is supported by prior studies (e.g., Taszarek et al., 2021; Pilguj et al., 2022), likely due to the its improved representation of moisture-related variables, especially in lower levels (Fig. 5f, Table 3). This advantage may be attributable to its high horizontal and vertical resolution (Hersbach et al., 2020), improved moisture sensitivity in deep convection (Virman et al., 2021), and assimilation of all-sky satellite observations (Geer et al., 2017).

Statistical analysis shows that NWP performance for dynamic parameters is highly sensitive to layer depth. For SRH, $SRH_{0\text{–}1km}$ exhibits median errors of around 6 m^2 s^{-2} and MAEs near 20 m^2 s^{-2} (Table 4), while $SRH_{0\text{–}3km}$ shows similar uncertainty but smaller median errors (Figs. 4e, f). For VWS, deeper-layer $VWS_{0\text{–}6km}$ shows little bias (−3 to 3 m s^{-1}), but $VWS_{0\text{–}1km}$ is consistently underestimated (Figs. 4g, h). Correlations between NWP data and observations of VWS improve with increasing shear layer depth: $VWS_{0\text{–}1km}$ ranges from 0.59 to 0.76, while $VWS_{0\text{–}6km}$ correlations reach 0.97 (Table 4). MW follows a similar trend of accuracy increasing with depth, with the correlation rising from 0.88 ($MW_{0\text{–}1km}$) to 0.95 ($MW_{0\text{–}6km}$) and the MAE dropping from 0.90 ($MW_{0\text{–}1km}$) to 0.64 ($MW_{0\text{–}6km}$). These results highlight persistent biases in near-surface parameters, likely due to limitations in boundary layer and topographical representation (Allen and Karoly, 2014; Taszarek et al., 2018; King and Kennedy, 2019).

Among the datasets, CRA-40 performs best for SRH, showing the highest correlations (0.88 and 0.92 for $SRH_{0\text{–}1km}$ and $SRH_{0\text{–}3km}$,) and lowest MAEs (18.0 m^2 s^{-2} and 20.0 m^2 s^{-2} for $SRH_{0\text{–}1km}$ and $SRH_{0\text{–}3km}$, respectively). Other datasets slightly overestimate SRH (Figs. 4e, f), exhibit larger MAEs, and show lower correlations (Table 4). CRA-40 also outperforms others in terms of VWS and MW, with strong correlations across all layers: 0.76–0.97 for VWS and 0.90–0.95 for MW (Table 4). Such a superior performance of CRA-40 stems from its better simulation of V and U winds (Table 3). A key factor is CRA-40's enhanced data assimilation, which includes not only WMO GTS data, but also additional observations from the CMA, including archived national and regional surface observations, field campaign radiosonde data, and Chinese AMDAR (Aircraft Meteorological Data Relay) data (Liu et al., 2023). This enhanced data assimilation, particularly over oceanic and land regions, substantially improves CRA-40's accuracy at lower levels. However, these enhancements have limited impact on thermodynamic variables, which depend on the full vertical profile.

Further investigation reveals that the performance of NWP data varies significantly across different parameter types, including thermodynamic parameters and dynamic parameters (Tables 3 and 4). For the thermodynamic parameters, which describe instability based on temperature and moisture profiles, the correlations between NWP data and observations are around 0.65 for SBCAPE, 0.60 for SBCIN, 0.8 for LCL, 0.46 for LFC, and 0.89 for EL, with the temperature profiles exhibiting higher correlations (Table 3). In contrast, dynamic parameters derived from wind profiles show even higher correlations, with deeper-layer SRH, VWS, and MW exceeding 0.9. These results suggest that NWP data are least reliable for moisture-related parameters, moderately reliable for temperature-related parameter, and most reliable for wind-related parameters. Moreover, in terms of the performance of the composite parameters, temporal changes are dominated by monthly fluctuations (Figs. 3 and 4) rather than interannual variability (not shown).

4. Impacts of upstream atmospheric errors on downstream convective system

Validation of the CTL experiment showed that the simulated daily and diurnal rainfall was stronger than that of IMERG observations over inland and coastal South China (Fig. 6), consistent with previous studies (Yang et al., 2004; Chen et al., 2016). This overestimation may result from coarser resolution, physics limitations, or misrepresentation of coastal flows (Zhang and Meng, 2019). Moreover, CTL used averaged FNL data and aimed to capture general rainfall features, while IMERG reflects real events. Thus, an exact match between the CTL-simulated rainfall and satellite-derived rainfall estimates was not expected. Despite the differences, CTL successfully reproduced key rainfall patterns, including the timing and location of rainfall anomalies: the late-night to morning positive anomaly of the coastal rainfall (Figs. 6b, g, e, j); the afternoon positive anomaly of the inland rainfall (Figs. 6c, i); and the centers of total rainfall over both coastal and inland areas.

Comparative analyses of the various sensitivity experiments identify the primary factors contributing to rainfall enhancement in these regions. For the offshore area south of Hainan Island, the experiments involving the reduction of temperature errors showed the most significant rainfall enhancement (Figs. 7a, b, d). This rainfall enhancement initiates in the early evening (Figs. 8c, g, o) and propagates offshore over the following 12 h (Figs. 8a, d, e, h, m, p), aligning with the offshore movement of the land breeze. Notably, FNL tends to underestimate the temperature below 700 hPa (Fig. 5e). Consequently, the error reduction procedure increases the low-level vertical temperature gradient over the ocean, leading to two primary effects: (1) enhanced instability over the NSCS, as indicated by increased CAPE

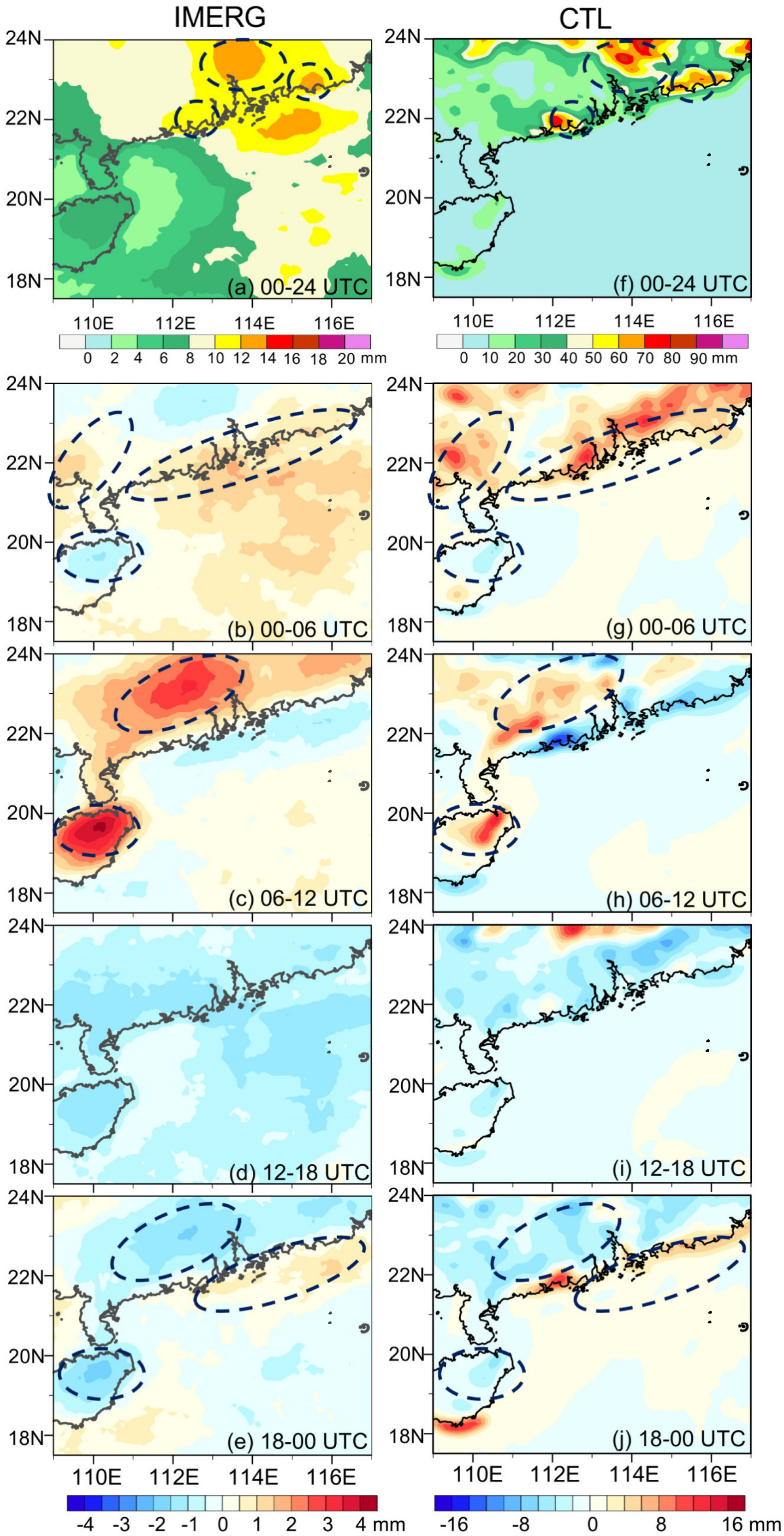

Fig. 6. Comparison between observations (IMERG) and CTL results: (a) daily rainfall averaged from April to September 2020–23; (b–e) diurnal rainfall accumulations every 6 h; (f–j) similar to (a–e) but for CTL. Note that the CTL results have been interpolated into IMERG grids.

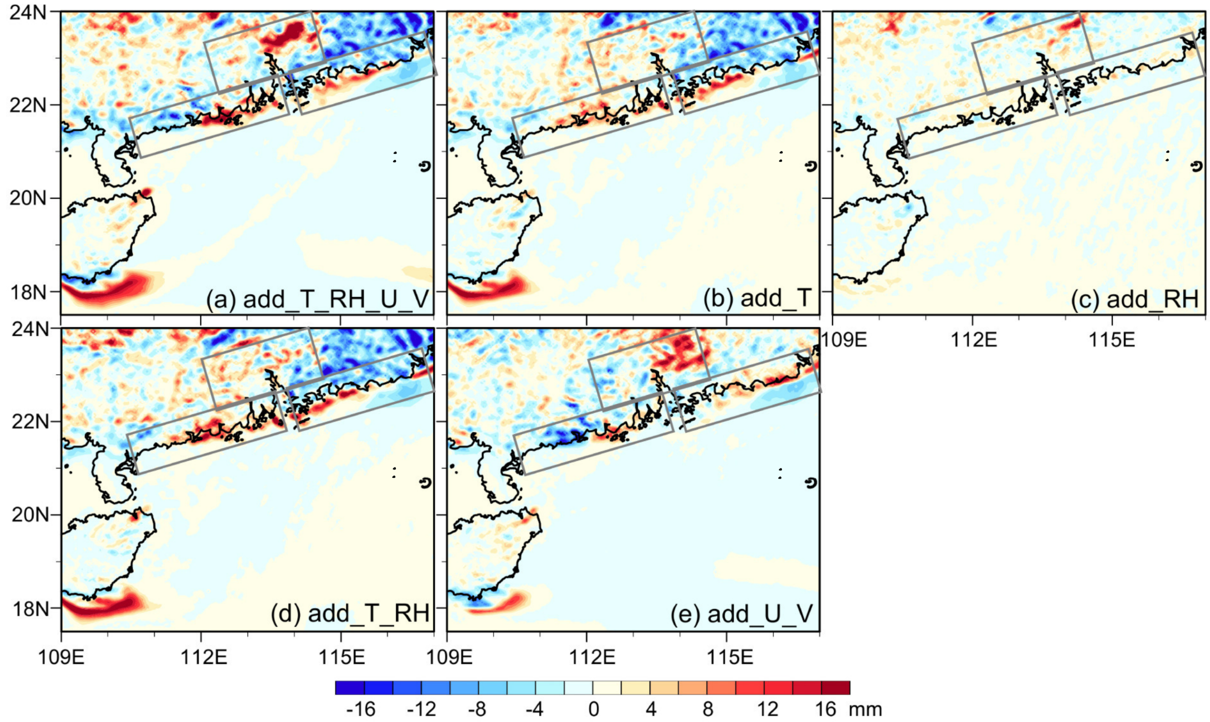

Fig. 7. Difference of daily cumulative precipitation between the (a) add_T_RH_U_V, (b) add_T, (c) add_RH, (d) add_T_RH, and (e) add_U_V experiments and the CTL experiment. The three grey boxes denote the rainfall hotspots as indicated in Fig. 1a.

(Figs. 9a, b, d), and moist static energy (not shown); and (2) intensified land breeze circulations due to a stronger nocturnal land–sea temperature contrast (Huang et al., 2024). These changes result in stronger and earlier coastal rainfall that subsequently propagates offshore. Rainfall production over the offshore regions of the east and west coast of South China exhibits similar characteristics and underlying mechanisms.

In contrast, the rainfall enhancement over the inland PRD can mainly be attributed to the reduction of errors in the dynamic wind fields (Figs. 7a, e). Significant rainfall enhancement is observed over the PRD from afternoon to midnight (Figs. 8r–t), associated with a weakened southerly wind (Fig. 9e), which favors the maintenance of local convection over the PRD region rather than southward propagation (Figs. 6g–i). Additionally, errors in RH have a comparatively smaller impact on rainfall production (Fig. 7c).

5. Concluding remarks

The coastal regions of southern China experience exceptional convection and associated rainfall, particularly during the warm season when the lower-tropospheric southerly winds bring moisture and momentum from the NSCS. Due to the sparseness of observations over the NSCS, NWP models face significant uncertainties. Leveraging long-term radiosonde measurements from NSCS islands, this study characterizes convective environments and evaluates five global NWP datasets (ERA5, MERRA-2, FNL, CRA-40, and JRA-3Q) in representing these conditions.

Systematic biases are revealed in NWP basic state variables below 950 hPa, featuring positive V wind biases and negative biases in U winds, Q_v, and temperature. The NWP data demonstrate better skill in representing mid-tropospheric LR ($LR_{0\text{–}3km}$, $LR_{700\text{–}500hPa}$), MW, VWS, and SRH over deeper layers (e.g., 0–3 km and 0–6 km). These low-level biases lead to underestimation in SBCAPE and EL, overestimation in LCL and SRH, and minimal bias in LR, SBCIN, VWS and MW. Moisture-related parameters (SBCAPE, CIN, EL, LCL, LFC) exhibit substantial variability, while LR remains relatively stable. This contrast suggests that the instability errors originate primarily from moisture field inaccuracies rather than temperature discrepancies. Uncertainties among NWP products arise from different model resolutions, sources of the input observations, parameterizations, and assimilation methods. Among the convective parameters and low-level variables, CRA-40 demonstrates the highest correlation and lowest MAEs for dynamic parameters, while ERA5 performs best in thermodynamic parameters.

Given the systematic biases in NWP model representations of the lower troposphere, multiple sensitivity numerical simulations were conducted to investigate how meteorological variable errors over the NSCS affect downstream rainfall production in coastal regions. The results demonstrate that rainfall patterns are significantly modulated when low-level thermodynamic and dynamic errors over upstream ocean are corrected, particularly over the offshore area of southern Hainan Island, coasts of China's mainland, and the PRD. The rainfall production on windward coasts is most sensitive

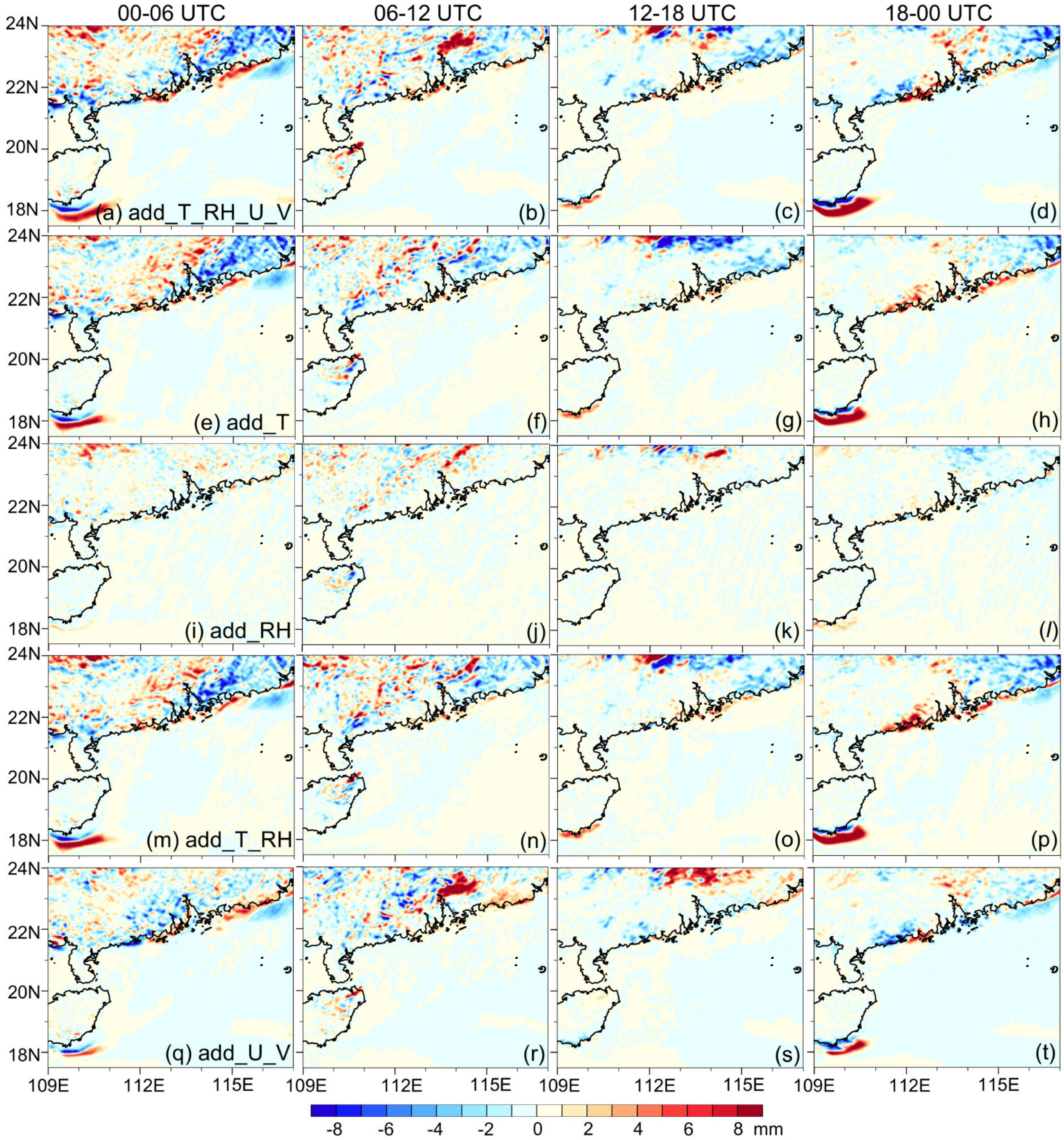

Fig. 8. Difference of diurnal precipitation between the (a–d) add_T_RH_U_V, (e–h) add_T, (i–l) add_RH, (m–p) add_T_RH, and (q–t) add_U_V experiments and the CTL experiment.

to the low-level air temperature errors during nocturnal hours, primarily through enhanced instability and amplified land–sea thermal contrast. The PRD, as a climatological rainfall hotspot, demonstrates strongest sensitivity to low-level wind errors, where weakened southerlies effectively block the southward propagation of inland convective systems. Notably, while higher resolution WRF simulations tend to produce stronger precipitation forecasts (e.g., Prein et al., 2015), which have also been noted in previous studies that used the same framework of composite simulation (e.g., Chen et al., 2016), this study emphasizes the variation in the spatial distributions of the precipitation rather than the absolute rainfall amount of individual synoptic events. The CTL experiment reasonably reproduced the overall rainfall patterns, providing a credible baseline for the sensitivity experiments, which adequately served the purpose of this investigation.

While reanalysis datasets provide valuable insights, notable limitations remain, particularly in the accurate representation of the atmospheric boundary layer. To address these gaps, additional field observations are urgently needed. These efforts should leverage existing observation platforms, including islands, aircrafts, and research vessels, to obtain high-resolution, in situ data. Furthermore, targeted

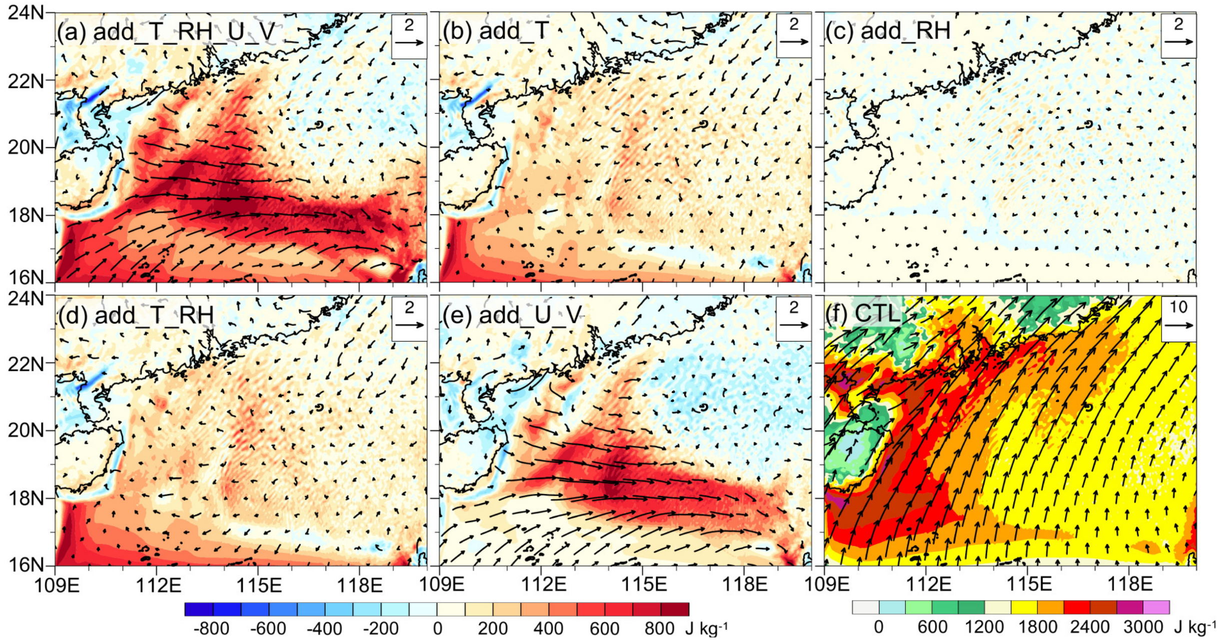

Fig. 9. Differences of CAPE and horizontal winds at 925 hPa between the (a) add_T_RH_U_V, (b) add_T, (c) add_RH, (d) add_T_RH, and (e) add_U_V experiments and the CTL experiment at 0000 UTC. Panel (f) is the CAPE from CTL.

field campaign experiments utilizing multi-source observational instruments, deployed on mobile platforms, are anticipated to significantly improve model depictions of lower-tropospheric conditions. Such advancements in the initial state for models are essential for enhancing the accuracy of short-term forecasts of severe weather events along the South China coast.

Acknowledgements. This research was supported by the National Natural Science Foundation of China (Grant Nos. 42030610, 42275006, 41805035, and 42305001), the Guangdong Basic and Applied Basic Research Foundation (Grant No. 2024A1515030210), the Guangdong Provincial Marine Meteorology Science Data Center (Grant No. 2024B1212070014), the Open Project of the Xiamen Key Laboratory of Straits Meteorology (Grant Nos. HXQX202304 and 2024KF02), and the Key Innovation Team of the China Meteorological Administration (Grant No. CMA2023ZD08).

Data availability statement MERRA-2 data are available at https://disc.gsfc.nasa.gov/. The NCEP FNL data, ERA5 and JRA-3Q data were downloaded from http://rda.ucar.edu. The CRA-40 data were downloaded from http://data.cma.cn/CRA.

REFERENCES

Allen, J. T., and D. J. Karoly, 2014: A climatology of Australian severe thunderstorm environments 1979–2011: Inter-annual variability and ENSO influence. *International Journal of Climatology*, **34**, 81−97, https://doi.org/10.1002/joc.3667.

Allen, J. T., and M. K. Tippett, 2015: The characteristics of United States hail reports: 1955-2014. *Electron. J. Severe Storms Meteor.*, **10**(3), 1−31, https://doi.org/10.55599/ejssm.v10i3.60.

Baidu, M., J. Schwendike, J. H. Marsham, and J. Bain, 2022: Effects of vertical wind shear on intensities of mesoscale convective systems over West and Central Africa. *Atmospheric Science Letters*, **23**, e1094, https://doi.org/10.1002/asl.1094.

Bao, X. H., and F. Q. Zhang, 2013: Evaluation of NCEP-CFSR, NCEP-NCAR, ERA-interim, and ERA-40 reanalysis datasets against independent sounding observations over the Tibetan Plateau. *J. Climate*, **26**, 206−214, https://doi.org/10.1175/JCLI-D-12-00056.1.

Bao, X. H., R. D. Xia, Y. L. Luo, and J. Yue, 2023: Efficiently improving ensemble forecasts of warm-sector heavy rainfall over coastal southern China: Targeted assimilation to reduce the critical initial field errors. *Journal of Meteorological Research*, **37**, 486−507, https://doi.org/10.1007/s13351-023-2140-8.

Chen, F., and J. Dudhia, 2001: Coupling an advanced land surface-hydrology model with the Penn State-NCAR MM5 modeling system. Part I: Model implementation and sensitivity. *Mon. Wea. Rev.*, **129**, 569−585, https://doi.org/10.1175/1520-0493(2001)129<0569:CAALSH>2.0.CO;2.

Chen, J., A. G. Dai, Y. C. Zhang, and K. L. Rasmussen, 2020: Changes in convective available potential energy and convective inhibition under global warming. *J. Climate*, **33**, 2025−2050, https://doi.org/10.1175/JCLI-D-19-0461.1.

Chen, X. C., F. Q. Zhang, and K. Zhao, 2016: Diurnal variations of the land-sea breeze and its related precipitation over South China. *Journal of the Atmospheric Sciences*, **73**, 4793−4815, https://doi.org/10.1175/JAS-D-16-0106.1.

Davies-Jones, R., D. W. Burgess, and M. P. Foster, 1990: Test of helicity as a tornado forecast parameter. Preprints, *16th Conf. on Severe Local Storms*, Kananaskis Park, Canada, Amer. Meteor. Soc., 588−592.

Davis, S. M., and Coauthors, 2017: Assessment of upper tropospheric and stratospheric water vapor and ozone in reanalyses as part of S-RIP. *Atmospheric Chemistry and Physics*, **17**, 12 743−12 778, https://doi.org/10.5194/acp-17-12743-2017.

Ding, Y. H., and J. C. L. Chan, 2005: The East Asian summer monsoon: An overview. *Meteorol. Atmos. Phys.*, **89**, 117–142, https://doi.org/10.1007/s00703-005-0125-z.

Du, Y., and G. X. Chen, 2019: Climatology of low-level jets and their impact on rainfall over southern China during the early-summer rainy season. *J. Climate*, **32**, 8813–8833, https://doi.org/10.1175/JCLI-D-19-0306.1.

Feng, Q., and Q. H. Zhang, 2018: Statistics of environmental vertical wind shear and water vapor field on the change of tropical cyclone structure in Northwest Pacific Ocean from 2001 to 2014. *Acta Scientiarum Naturalium Universitatis Pekinensis*, **54**, 713–720, https://doi.org/10.13209/j.0479-8023.2017.141. (in Chinese with English abstract)

Fu, S. M., J. P. Zhang, Y. L. Luo, W. T. Yang, and J. H. Sun, 2022: Energy paths that sustain the warm-sector torrential rainfall over South China and their contrasts to the frontal rainfall: A case study. *Adv. Atmos. Sci.*, **39**(9), 1519–1535, https://doi.org/10.1007/s00376-021-1336-z.

Gao, X. Y., Y. L. Luo, Y. L. Lin, and X. H. Bao, 2022: A source of WRF simulation error for the early-summer warm-sector heavy rainfall over South China coast: Land-sea thermal contrast in the boundary layer. *J. Geophys. Res.*, **127**, e2021JD035179, https://doi.org/10.1029/2021JD035179.

Geer, A. J., and Coauthors, 2017: The growing impact of satellite observations sensitive to humidity, cloud and precipitation. *Quart. J. Roy. Meteor. Soc.*, **143**, 3189–3206, https://doi.org/10.1002/qj.3172.

Gelaro, R., and Coauthors, 2017: The modern-era retrospective analysis for research and applications, version 2 (MERRA-2). *J. Climate*, **30**, 5419–5454, https://doi.org/10.1175/JCLI-D-16-0758.1.

Grell, G. A., and D. Dévényi, 2002: A generalized approach to parameterizing convection combining ensemble and data assimilation techniques. *Geophys. Res. Lett.*, **29**, 1693, https://doi.org/10.1029/2002GL015311.

Harada, Y., S. Kobayashi, Y. Kosaka, J. Chiba, and T. Tokuhiro, 2021: Early results of the evaluation of the JRA-3Q reanalysis. *Proc. EGU General Assembly Conf.*, EGU21-3762, https://doi.org/10.5194/egusphere-egu21-3762.

Hersbach, H., and Coauthors, 2020: The ERA5 global reanalysis. *Quart. J. Roy. Meteor. Soc.*, **146**, 1999–2049, https://doi.org/10.1002/qj.3803.

Hong, S.-Y., J. Dudhia, and S.-H. Chen, 2004: A revised approach to ice microphysical processes for the bulk parameterization of clouds and precipitation. *Mon. Wea. Rev.*, **132**, 103–120, https://doi.org/10.1175/1520-0493(2004)132<0103:ARATIM>2.0.CO;2.

Hong, S.-Y., Y. Noh, and J. Dudhia, 2006: A new vertical diffusion package with an explicit treatment of entrainment processes. *Mon. Wea. Rev.*, **134**, 2318–2341, https://doi.org/10.1175/MWR3199.1.

Huang, L., and Y. L. Luo, 2017: Evaluation of quantitative precipitation forecasts by TIGGE ensembles for South China during the presummer rainy season. *J. Geophys. Res.*, **122**, 8494–8516, https://doi.org/10.1002/2017JD026512.

Huang, L., L. Q. Bai, and Y. J. Zhang, 2024: Analysis of uncertainties in convection-permitting ensemble simulations of land breeze and nocturnal coastal rainfall in South China. *Journal of Meteorological Research*, **38**(6), 1047–1063, https://doi.org/10.1007/s13351-024-4075-0.

King, A. T., and A. D. Kennedy, 2019: North American supercell environments in atmospheric reanalyses and RUC-2. *J. Appl. Meteorol. Climatol.*, **58**, 71–92, https://doi.org/10.1175/JAMC-D-18-0015.1.

Kosaka, Y., and Coauthors, 2024: The JRA-3Q reanalysis. *J. Meteor. Soc. Japan*, **102**, 49–109, https://doi.org/10.2151/jmsj.2024-004.

Lee, J. W., 2002: Tornado proximity soundings from the NCEP/NCAR reanalysis data. M.S. thesis, University of Oklahoma, 61 pp.

Li, C. F., and M. Yanai, 1996: The onset and interannual variability of the Asian summer monsoon in relation to land-sea thermal contrast. *J. Climate*, **9**, 358–375, https://doi.org/10.1175/1520-0442(1996)009<0358:TOAIVO>2.0.CO;2.

Li, F. N., D. R. Chavas, K. A. Reed, and D. T. Dawson II, 2020: Climatology of severe local storm environments and synoptic-scale features over North America in ERA5 reanalysis and CAM6 simulation. *J. Climate*, **33**, 8339–8365, https://doi.org/10.1175/JCLI-D-19-0986.1.

Li, Z. Y., J. H. Wei, X. H. Bao, and Y. Q. Sun, 2023: Intercomparison of tropospheric and stratospheric mesoscale kinetic energy resolved by the high-resolution global reanalysis datasets. *Quart. J. Roy. Meteor. Soc.*, **149**, 3738–3764, https://doi.org/10.1002/qj.4605.

Liu, Z. Q., and Coauthors, 2023: CRA-40/Atmosphere—The first-generation Chinese atmospheric reanalysis (1979-2018): System description and performance evaluation. *Journal of Meteorological Research*, **37**(1), 1–19, https://doi.org/10.1007/s13351-023-2086-x.

Manney, G. L., and Coauthors, 2017: Reanalysis comparisons of upper tropospheric-lower stratospheric jets and multiple tropopauses. *Atmospheric Chemistry and Physics*, **17**, 11 541–11 566, https://doi.org/10.5194/acp-17-11541-2017.

Markowski, P. M., J. M. Straka, E. N. Rasmussen, and D. O. Blanchard, 1998: Variability of storm-relative helicity during VORTEX. *Mon. Wea. Rev.*, **126**, 2959–2971, https://doi.org/10.1175/1520-0493(1998)126<2959:VOSRHD>2.0.CO;2.

Mlawer, E. J., S. J. Taubman, P. D. Brown, M. J. Iacono, and S. A. Clough, 1997: Radiative transfer for inhomogeneous atmospheres: RRTM, a validated correlated-k model for the longwave. *J. Geophys. Res.*, **102**, 16 663–16 682, https://doi.org/10.1029/97JD00237.

National Centers for Environmental Prediction/National Weather Service/NOAA/U. S. Department of Commerce, 2000: NCEP FNL operational model global tropospheric analyses, continuing from July 1999. Research Data Archive at the National Center for Atmospheric Research, Computational and Information Systems Laboratory, https://doi.org/10.5065/D6M043C6.

Niu, G.-Y., and Coauthors, 2011: The community Noah land surface model with multiparameterization options (Noah-MP): 1. Model description and evaluation with local-scale measurements. *J. Geophys. Res.*, **116**, D12109, https://doi.org/10.1029/2010JD015139.

Pilguj, N., M. Taszarek, J. T. Allen, and K. A. Hoogewind, 2022: Are trends in convective parameters over the united states and Europe consistent between reanalyses and observations. *J. Climate*, **35**, 3605–3626, https://doi.org/10.1175/JCLI-D-21-0135.1.

Prein, A. F., and Coauthors, 2015: A review on regional convection-permitting climate modeling: Demonstrations, prospects, and challenges. *Rev. Geophys.*, **53**, 323–361, https://doi.org/10.1002/2014RG000475.

Rädler, A. T., P. Groenemeijer, E. Faust, and R. Sausen, 2018:

Detecting severe weather trends using an additive regressive convective hazard model (AR-CHaMo). *J. Appl. Meteorol. Climatol.*, **57**, 569–587, https://doi.org/10.1175/JAMC-D-17-0132.1.

Shen, C., J. L. Zha, J. Wu, D. M. Zhao, C. Azorin-Molina, W. X. Fan, and Y. Yu, 2022: Does CRA-40 outperform other reanalysis products in evaluating near-surface wind speed changes over China. *Atmospheric Research*, **266**, 105948, https://doi.org/10.1016/j.atmosres.2021.105948.

Skamarock, W. C., and Coauthors, 2008: A description of the advanced research WRF version 3. NCAR Tech. Note TN-4751STR, 113 pp.

Sun, J. H., and F. Q. Zhang, 2012: Impacts of mountain-plains solenoid on diurnal variations of rainfalls along the Mei-Yu front over the East China plains. *Mon. Wea. Rev.*, **140**, 379–397, https://doi.org/10.1175/MWR-D-11-00041.1.

Sun, J. H., Y. C. Zhang, R. X. Liu, S. M. Fu, and F. Y. Tian, 2019: A review of research on warm-sector heavy rainfall in China. *Adv. Atmos. Sci.*, **36**, 1299–1307, https://doi.org/10.1007/s00376-019-9021-1.

Taszarek, M., H. E. Brooks, and B. Czernecki, 2017: Sounding-derived parameters associated with convective hazards in Europe. *Mon. Wea. Rev.*, **145**, 1511–1528, https://doi.org/10.1175/MWR-D-16-0384.1.

Taszarek, M., H. E. Brooks, B. Czernecki, P. Szuster, and K. Fortuniak, 2018: Climatological aspects of convective parameters over Europe: A comparison of ERA-interim and sounding data. *J. Climate*, **31**, 4281–4308, https://doi.org/10.1175/JCLI-D-17-0596.1.

Taszarek, M., J. T. Allen, T. Púčik, K. A. Hoogewind, and H. E. Brooks, 2020: Severe convective storms across Europe and the United States. Part II: ERA5 environments associated with lightning, large hail, severe wind, and tornadoes. *J. Climate*, **33**, 10 263–10 286, https://doi.org/10.1175/JCLI-D-20-0346.1.

Taszarek, M., N. Pilguj, J. T. Allen, V. Gensini, H. E. Brooks, and P. Szuster, 2021: Comparison of convective parameters derived from ERA5 and MERRA-2 with rawinsonde data over Europe and North America. *J. Climate*, **34**, 3211–3237, https://doi.org/10.1175/JCLI-D-20-0484.1.

Thompson, R. L., R. Edwards, J. A. Hart, K. L. Elmore, and P. Markowski, 2003: Close proximity soundings within supercell environments obtained from the Rapid Update Cycle. *Wea. Forecasting*, **18**, 1243–1261, https://doi.org/10.1175/1520-0434(2003)018<1243:CPSWSE>2.0.CO;2.

Tippett, M. K., C. Lepore, and J. E. Cohen, 2016: More tornadoes in the most extreme U.S. tornado outbreaks. *Science*, **354**, 1419–1423, https://doi.org/10.1126/science.aah7393.

Tootill, D., and D. J. Kirshbaum, 2022: Ensemble sensitivity of precipitation type to initial conditions for a major freezing rain event in Montreal. *Mon. Wea. Rev.*, **150**, 1761–1780, https://doi.org/10.1175/MWR-D-21-0254.1.

Varga, Á. J., and H. Breuer, 2022: Evaluation of convective parameters derived from pressure level and native ERA5 data and different resolution WRF climate simulations over Central Europe. *Climate Dyn.*, **58**, 1569–1585, https://doi.org/10.1007/s00382-021-05979-3.

Virman, M., M. Bister, J. Räisänen, V. A. Sinclair, and H. Järvinen, 2021: Radiosonde comparison of ERA5 and ERA-Interim reanalysis datasets over tropical oceans. *Tells*, **73**, 1–7, https://doi.org/10.1080/16000870.2021.1929752.

Wu, J. Y., and Coauthors, 2024: Can ERA5 reanalysis data characterize the pre-storm environment. *Atmospheric Research*, **297**, 107108, https://doi.org/10.1016/j.atmosres.2023.107108.

Yang, J. X., M. T. Huang, and P. M. Zhai, 2021: Performance of the CRA-40/land, CMFD, and ERA-interim datasets in reflecting changes in surface air temperature over the Tibetan Plateau. *Journal of Meteorological Research*, **35**, 663–672, https://doi.org/10.1007/s13351-021-0196-x.

Yang, M.-J., B. J.-D. Jou, S.-C. Wang, J.-S. Hong, P.-L. Lin, J.-H. Teng, and H.-C. Lin, 2004: Ensemble prediction of rainfall during the 2000-2002 Mei-Yu seasons: Evaluation over the Taiwan area. *J. Geophys. Res.*, **109**, D18203, https://doi.org/10.1029/2003JD004368.

Yin, J. F., X. Liang, Y. Xie, and Coauthors, 2023: East Asia reanalysis system (EARS). *Earth System Science Data*, **15**, 2329–2346, https://doi.org/10.5194/essd-15-2329-2023.

Yu, X. J., L. X. Zhang, T. J. Zhou, and J. W. Liu, 2021: The Asian subtropical westerly jet stream in CRA-40, ERA5, and CFSR reanalysis data: Comparative assessment. *Journal of Meteorological Research*, **35**, 46–63, https://doi.org/10.1007/s13351-021-0107-1.

Zhang, J. P., and Coauthors, 2021: Evaluation of surface relative humidity in China from the CRA-40 and current reanalyses. *Adv. Atmos. Sci.*, **38**, 1958–1976, https://doi.org/10.1007/s00376-021-0333-6.

Zhang, M. R., and Z. Y. Meng, 2019: Warm-sector heavy rainfall in southern China and its WRF simulation evaluation: A low-level-jet perspective. *Mon. Wea. Rev.*, **147**, 4461–4480, https://doi.org/10.1175/MWR-D-19-0110.1.

Zhou, Z. L., S. Chen, Z. Li, and Y. M. Luo, 2023: An evaluation of CRA40 and ERA5 precipitation products over China. *Remote Sensing*, **15**, 5300, https://doi.org/10.3390/rs15225300.